Spectral Decomposition and High-Accuracy Green's Functions: Overcoming the Nyquist-Shannon Limit via Complex-time Krylov Expansion

S. Paeckel
Department of Physics, Arnold Sommerfeld Center of Theoretical Physics, University of Munich, Theresienstrasse 37, 80333 Munich, Germany and Munich Center for Quantum Science and Technology (MCQST), Schellingstrasse 4, 80799 München, Germany

(Received 18 February 2025; revised 14 December 2025; accepted 16 March 2026; published 21 April 2026)

The accurate computation of low-energy spectra of strongly correlated quantum many-body systems, typically accessed via Green's functions, is a long-standing problem posing enormous challenges to numerical methods. When the spectral decomposition is obtained from Fourier transforming a time series, the Nyquist-Shannon theorem limits the frequency resolution $\Delta\omega$ according to the numerically accessible time domain size T via $\Delta\omega = 2\pi/T$. In tensor network methods, increasing the domain size is exponentially hard due to the ubiquitous spread of correlations, limiting the frequency resolution and thereby restricting this ansatz class mostly to one-dimensional systems with small quasiparticle velocities. Here, we show how this limitation can be overcome by augmenting the time series with complex-time Krylov states. With the example of the critical $S-1/2$ Heisenberg model and light bipolarons in the two-dimensional Su-Schrieffer-Heeger model, we demonstrate the enormous improvements in accuracy, which can be achieved using this method.

DOI: 10.1103/bx76-hps4

Introduction—The ability to compute the low-energy spectra of strongly correlated quantum many-body systems is of paramount importance in nearly every area of condensed matter physics. In particular, the direct relation between spectral functions and Green's functions has proven extremely fruitful to foster our understanding of condensed matter systems. This is based on the fact that spectral functions are directly accessible via various experimental probes such as ARPES, x-ray, and neutron scattering, while Green's functions are mathematical objects probing the many-body spectrum of the underlying Hamiltonians [1–9]. Moreover, Green's functions are the essential building blocks of the most successful methods for determining effective model Hamiltonians for the description of real materials [10–26].

The computation of Green's functions spans complementary frameworks. Diagrammatic and functional approaches provide controlled expansions in weak-coupling regimes [27]. Generalizations of density-functional theory [28,29] are highly successful but rely on the availability of proper exchange functionals, while nonperturbative cluster embedding schemes are also applicable in the presence of strong correlations [30–32].

Numerical methods provide an alternative route to dealing with strongly correlated systems [33–37]. Among these tensor networks (TNs) [38,39] are the defacto standard for one-dimensional systems, while Monte Carlo [40,41] is extraordinarily efficient in higher dimensions, yet suffers from the sign problem, especially for fermionic systems. Superficially, this methodical imbalance is attributed to the area law of entanglement, which, in two and higher dimensions, implies that already the representation of ground states exhibits an exponential scaling of the computational complexity [42,43]. However, the situation is even worse for TN-based approaches because Green's functions are typically computed from time evolutions of excited states and real-time simulations are limited by the ubiquitous spread of correlations [44]. It is this additional growth of entanglement under time evolution which drastically challenges their applicability to the computation of Green's functions in higher dimensions. In this Letter, we introduce a novel approach combining real- and complex-time evolutions to overcome this limitation. At the example of the critical $S-1/2$ Heisenberg chain and light bipolaron formation in the two-dimensional Su-Schrieffer-Heeger (SSH) model, we demonstrate the ability to significantly improve the frequency resolution of Green's functions, even for the case of two-dimensional systems.

Method—We consider a general frequency-dependent Green's function,

$$G_{AB}(\omega) = -\mathrm{i}\langle\varphi_A|(H - E_0 - \omega - \mathrm{i}\eta)^{-1}|\varphi_B\rangle, \qquad (1)$$

Published by the American Physical Society under the terms of the Creative Commons Attribution 4.0 International license. Further distribution of this work must maintain attribution to the author(s) and the published article's title, journal citation, and DOI.

where $|\varphi_A\rangle, |\varphi_B\rangle$ are excited states and $\hat{H}$ denotes the Hamiltonian of the system under consideration with ground-state energy E_0. To regularize the poles of G_{AB}, a finite broadening $\eta > 0$ is introduced. In TN simulations, G_{AB} typically is computed by simulating the real-time analogon and performing a Fourier transformation to frequency space

$$G_{AB}(\omega) = \lim_{T\to\infty} \int_0^T dt \langle\varphi_A|\hat{U}(t,\omega)|\varphi_B\rangle, \tag{2}$$

where we introduced $\hat{U}(t,\omega) = \mathrm{e}^{-\mathrm{i}(\hat{H}-E_0-\omega-\mathrm{i}\eta)t}$ for convenience. In practice, the time T that can be reached is limited, such that the broadening η has to be chosen to be of the order of $2\pi/T$ to smear out unphysical artifacts arising from the Fourier transformation on the finite time domain. Let us recast Eq. (2) by exploiting the group property of $\hat{U}(t,\omega)$ and splitting the integration domain into smaller intervals of size T, i.e., $\mathbb{R}_0^+ = [0,T) \cup [T,2T) \cup \cdots$. We then introduce the operator $\hat{S}(T,\omega) = \sum_{p=0}^{\infty} [\hat{U}(T,\omega)]^p$, which boosts the evolution on the finite interval $[0,T)$ to all intervals $[pT,\{p+1\}T)$ such that

$$G_{AB}(\omega) = \int_0^T dt \langle\varphi_A|\hat{U}(t,\omega)\hat{S}(T,\omega)|\varphi_B\rangle. \tag{3}$$

The geometric series in $\hat{S}(T,\omega)$ always converges as long as $\eta T > 0$, while a truncation at zeroth order $p = 0$ yields $\hat{S} = 1$, and one recovers the usual finite-time integration over the domain $[0,T]$. In that case, the Nyquist-Shannon theorem [45,46] dictates that only an approximation to the Green's function $\tilde{G}_{AB}^T(\omega = \omega_k)$ sampled at frequencies $\omega_k = (2\pi/T)k \equiv k\Delta\omega$ $(k \in \mathbb{Z})$ is obtained. It is now convenient to define $\hat{K} = \hat{S} - 1$. This allows for decomposing the full Green's function into the $p = 0$ part $\tilde{G}_{AB}^T$ and a correction K_{AB}^T:

$$G_{AB} = \tilde{G}_{AB}^T + K_{AB}^T, \tag{4}$$

$$K_{AB}^T = \int_0^T dt \langle\varphi_A|\hat{U}(t,\omega)\hat{K}(T,\omega)|\varphi_B\rangle. \tag{5}$$

By harnessing additional information about the spectral properties encoded in $K_{AB}^T(\omega)$, faint signals also can be recovered, contrasting this approach to compressed sensing schemes [47,48]. The task is now to determine K_{AB}^T, and we show in the following how this contribution can be approximated efficiently using TNs.

The key observation is that K_{AB}^T accounts for the low-frequency part of G_{AB}. In fact, setting $\hat{S} \equiv 1$ essentially introduces a low-pass filter on the time domain such that the Green's function in frequency space is fully determined from equally spaced samples $\tilde{G}_{AB}^T(\omega_k)$ [45,46]. Therefore, information about the dependency of G_{AB} on smaller frequencies $\omega \in [0,\Delta\omega]$ must be encoded in K_{AB}^T. Moreover, the Green's function typically exhibits a finite spectral width, i.e., it is nonzero only in a finite frequency interval because the states $|\varphi_\mu\rangle$ with $\mu = A, B$ are mostly obtained from local excitations above the ground state of $\hat{H}$. Thus, $\hat{K}(T,\omega)$ is ideally evaluated in a low-energy subspace.

In general, low-energy subspaces are obtained by constructing Krylov spaces via successively applying $\hat{H}$ to proper initial states $|\varphi_\mu\rangle$. However, the low-energy resolution in such a Krylov space converges slowly for critical systems or those with small gaps, hence limiting the applicability significantly [49–51]. We therefore pursue another approach of building a Krylov space from time evolving the initial states along a complex contour of segments $\tau = [1 - \mathrm{i}\tan(\alpha)]\delta t$. The time-evolution operator for each segment can be decomposed as

$$\hat{U}_\tau = \mathrm{e}^{-\hat{H}\delta t\tan(\alpha)}\mathrm{e}^{-\mathrm{i}\hat{H}\delta t} \tag{6}$$

for a complex angle $\alpha \in [0,\pi/2)$. Here, the role of the exponential damping $\mathrm{e}^{-\hat{H}\delta t\tan(\alpha)}$ is to suppress higher energy contributions such that the Krylov space,

$$\mathcal{H}_\mu^{D\tau} = \mathrm{span}\left\{\frac{|\varphi_\mu\rangle}{\||\varphi_\mu\rangle\|}, \frac{\hat{U}_\tau|\varphi_\mu\rangle}{\|\hat{U}_\tau|\varphi_\mu\rangle\|}, \ldots, \frac{\hat{U}_\tau^{D-1}|\varphi_\mu\rangle}{\|\hat{U}_\tau^{D-1}|\varphi_\mu\rangle\|}\right\}, \tag{7}$$

is spanned by normalized states that exhibit a large overlap with the low-energy eigenstates of $\hat{H}$.

The complex contour has immediate effects on the efficiency of TN methods. The continuous suppression of high-energy states yields a significant reduction of bond dimension upon time evolving the initial states. This has been exploited only recently to improve the efficiency of time evolutions, yet the complex time was promoted to a complex frequency by a direct Fourier transform, requiring further postprocessing or evaluations of expensive auxiliary quantities to obtain real-frequency data [52,53]. By contrast, in our approach we use the complex-time Krylov space $\mathcal{H}_\mu^{D\tau}$ to expand the Hamiltonian $\hat{H}$ directly. Approximating $\hat{K}(T,\omega)$ on the real frequency axis then allows for evaluating the time integration in the $T \to \infty$ limit facilitating arbitrary frequency resolution.

Given a collection of states $\{|\varphi_B^0\rangle, |\varphi_B^1\rangle, \ldots\}$ generated via complex-time evolution of the initial state $|\varphi_B^n\rangle = \hat{U}_{n\tau}|\varphi_B\rangle/\|\hat{U}_{n\tau}|\varphi_B\rangle\|$, the following steps are required to evaluate K_{AB}^T: (1) Construct the Gram matrix $\mathbf{M}$ with elements $M_{nm} = \langle\varphi_B^n|\varphi_B^m\rangle$ (and denote by $\vec{M}_m$ the mth column vector of $\mathbf{M}$). (2) Diagonalize $\mathbf{M} = \mathbf{U}\mathbf{D}\mathbf{U}^\dagger$ and compute $\mathbf{X} = \mathbf{U}\mathbf{D}^{-\frac{1}{2}}$ to get a transformation into an orthonormal basis $|\psi_B^i\rangle = \sum_{n=1}^r X_{ni}|\varphi_B^n\rangle$. If there are eigenvalues

$D_{ii} \leq 0$, discard them to ensure the basis has full rank $r \leq D$. (3) Compute $\tilde{H}^{\text{eff}}_{nm} = \langle \varphi^n_B | \hat{H} | \varphi^m_B \rangle$ and transform the matrix representation of the effective Hamiltonian $\tilde{\mathbf{H}}^{\text{eff}}$ into the orthonormal basis $H^{\text{eff}}_{ij} = \langle \psi^i_B | \hat{H} | \psi^j_B \rangle = (\mathbf{X}^* \tilde{\mathbf{H}}^{\text{eff}} \mathbf{X}^t)_{ij}$. (4) Compute $Y_{AB,n}(t) = \langle \varphi_A(-t) | \varphi^n_B \rangle$, where $|\varphi_A(t)\rangle$ are the real-time evolutions of $|\varphi^A\rangle$.

Using the eigendecomposition $\mathbf{H}^{\text{eff}} = \mathbf{Q}\mathbf{E}^{\text{eff}}\mathbf{Q}^\dagger$, the final expression for $K^T_{AB}(\omega)$ is given by

$$K^T_{AB}(\omega) = \int_0^T dt \vec{Y}_{AB}(t) e^{i(E_0+\omega+i\eta)t} \mathbf{X}\mathbf{Q} \frac{e^{-i(\mathbf{E}^{\text{eff}}-E_0-\omega-i\eta)T}}{1-e^{-i(\mathbf{E}^{\text{eff}}-E_0-\omega-i\eta)T}} \mathbf{Q}^\dagger \mathbf{X}^\dagger \vec{M}_0. \tag{8}$$

The costs to evaluate Eq. (8) are dominated by the scalar products to obtain M_{nm}, $\tilde{H}^{\text{eff}}_{nm}$ and $Y_{AB,n}(t)$. Here, the most expensive part is the computation of the $Y_{AB,n}(t)$ s, which have to be done for all real- and complex-time evolved states $|\varphi_A(t)\rangle$ and $|\varphi^m_B\rangle$, respectively. Luckily, these are all independent of each other and can be parallelized trivially, and the actual TN operations to evaluate overlaps are subleading compared to the time evolutions [54].

The convergence of the Green's function augmented by the complex-time Krylov space correction Eq. (8) can be analyzed in terms of Arnoldi iterations. A rigorous upper bound for the approximation error is derived in [55] yielding the practically relevant noise threshold

$$R \lesssim \frac{2}{\delta t \eta D} h_{r,r-1}, \tag{9}$$

where $h_{r,r-1}$ is the Arnoldi residual, which can be computed directly from $\mathbf{H}_{\text{eff}}$, and D denotes the spectral width of G_{AB} [60]. Crucially, $h_{r,r-1}$ is exponentially suppressed $\sim e^{r(1+\ln(\eta\tilde{\lambda}))}$ as long as $\ln(\delta t\tilde{\lambda}) < -1$, where $\tilde{\lambda}$ is the spectral width of $|\varphi_B\rangle$. Thus, for large rank r of the Gram matrix as well as small time steps δt, an exponential convergence toward the exact Green's function can be expected. Increasing the complex angle α is also beneficial, yet care must be taken: $\alpha > 0.1$ should be avoided to prevent numerical instabilities and to ensure linear independence for the Krylov states, i.e., sufficiently large r.

$S-1/2$ Heisenberg chain—As a first test case, we consider Green's functions of the isotropic $S-1/2$ Heisenberg chain:

$$\hat{H} = \sum_j \hat{\vec{S}}_j \hat{\vec{S}}_{j+1}. \tag{10}$$

The model is critical, i.e., there are gapless spinon excitations challenging most Krylov expansion schemes. To faithfully study the effect of incorporating the contributions $K^T_{AB}(\omega)$, we set the system size to $L = 16$ spins, which can be solved numerically exactly.

We computed the dynamical spin-structure factor (DSF) $A(k,\omega) = -(1/\pi)\,\text{Im}\,G_{zz}(k,\omega)$, where

$$G_{zz}(k,\omega) = \langle k | \left[\hat{H} - E_0 - \omega - i\eta\right]^{-1} | k \rangle \tag{11}$$

and $|k\rangle = (1/\sqrt{L})\sum_j e^{-ikr_j}\hat{S}^z_j|E_0\rangle$ is a longitudinal momentum space excitation of the ground state $|E_0\rangle$. Using a matrix-product state (MPS) representation [38,61–63], we performed real-time simulations [54] of the excited states $|k\rangle$ until time $T = 8$, corresponding to the time frame in which a spinon excitation traverses the system. Since spinons can scatter off each other, larger simulation times yield a significant increase of correlations, which in more complex systems would cause an exponential growth in the MPS bond dimension at a fixed truncation error [54] (here we allowed $\delta = 10^{-10}$ as the maximal discarded weight per site). It is exactly this breakdown of TN based methods which we alleviate by limiting the real-time evolution and instead involve Eq. (8).

To evaluate Eq. (8), we performed complex-time evolutions of the initial states for several complex angles α until a maximum time $\text{Re}(T_{\text{cplx}}) = 128$. For each value of α, we then constructed the Krylov subspace from maximally $D = 129$ time evolved states (including the initial state $|k\rangle$) using an equally spaced grid along the complex-time contour with $\delta t = 1$. The DSF is then obtained from Eq. (8), and we chose a broadening $\eta = 0.1$.

In Fig. 1(a) we compare against the numerically exact DSF (red). The curve with $\alpha = 0$ shows results using the finite-time integration, only. Note the artificial oscillations as well as the stark deviations in the peak height at $\omega = 0$. This is also indicated by the color-coded baseline displaying the absolute difference to the exact DSF. Note that, as soon as $K^T_{AB}(\omega)$ is added (finite α), the oscillations disappear, which is an immediate consequence of the fact that by incorporating Eq. (3) we work in the limit $T \to \infty$. Furthermore, even for the largest complex angle $\alpha = 0.05\pi$, the low-frequency behavior of the DSF is already well captured, and deviations are visible only at larger frequencies $\omega > 1$. These errors vanish when decreasing α, until for $\alpha = 0.02\pi$ we find excellent agreement, which is demonstrated in Fig. 1(b), too. In the left inset the computational benefits are shown by comparing the maximum bond dimension during the complex-time evolution to that occurring in a conventional real-time evolution. We also tested the quality of the approximation of $\hat{K}$ by

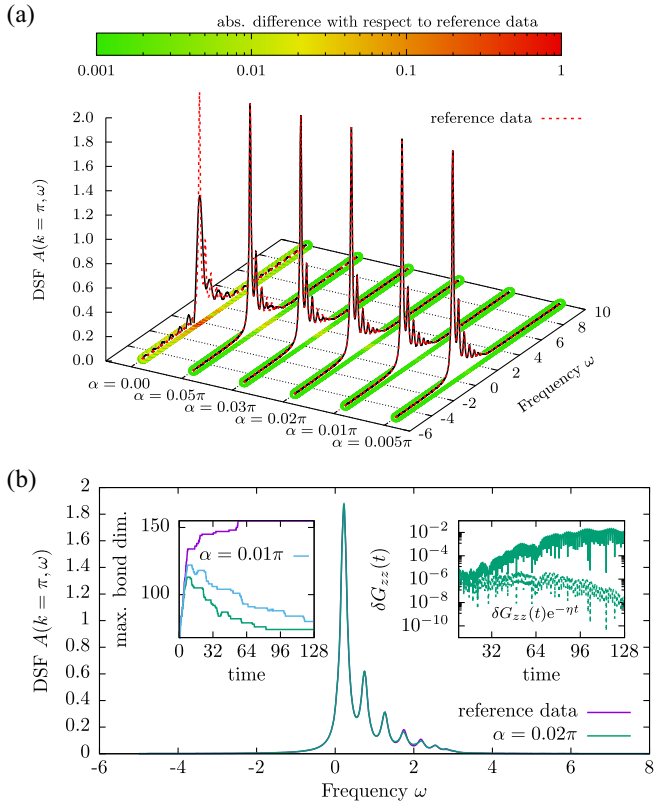


FIG. 1. (a) Comparison between DSFs of the $S-1/2$ Heisenberg model for different complex angles α (black) and a maximum complex simulation time $\mathrm{Re}(T_{\mathrm{cplx}}) = 128$ with exact reference data (red). Real-time evolution was done until $T = 8$, and $\alpha = 0$ shows the uncorrected DSF. The absolute difference between the complex time and the exact reference data is indicated by the color-coded baselines. (b) DSF for $\alpha = 0.02\pi$ to illustrate the precision of the corrected Green's function. Left inset: the bond dimensions of the complex-time evolution (green, blue) compared to the real case (purple). Right inset: the error of the local time-dependent Green's function when propagating the time evolution beyond $T = 8$ using the boost operator $\hat{S}(T,\omega)$ (solid line) and after incorporating the damping (dashed line) generated by the finite broadening $\eta = 0.1$.

explicitly forecasting the dynamics of the local excitations. In the right inset we plot the absolute error of the dynamics of the time-dependent Green's function $G_{zz}(t) = \langle E_0|\hat{S}^z_8(t)\hat{S}^z_8|E_0\rangle$ starting the prediction at time $T = 8$. Note that even at very long times $T > 100$ the errors are small $\lesssim 10^{-2}$, and in particular revivals caused from finite size effects, i.e., reflections of spinon excitations at the boundaries, are treated correctly such that incorporating the damping (dashed line) yields extremely high precision.

Two-dimensional SSH model—We now turn to a more challenging test case to demonstrate the power of our method. We study isolated two-electron bound states (bipolarons) in the Peierls SSH model [64–66] on a two-dimensional square lattice, in which electrons couple nonlocally to optical phonons. The Hamiltonian is given by

$$\hat{H} = -\sum_{\langle\vec{r},\vec{r}'\rangle}\sum_{\sigma}\left(\hat{c}^{\dagger}_{\vec{r},\sigma}\hat{c}_{\vec{r}',\sigma} + \mathrm{H.c.}\right)\left(t - g\hat{V}_{\vec{r},\vec{r}'}\right) + U\sum_{\vec{r}}\hat{n}_{\vec{r},\uparrow}\hat{n}_{\vec{r},\downarrow} + \Omega\sum_{\vec{r}}\hat{a}^{\dagger}_{\vec{r}}\hat{a}_{\vec{r}}, \tag{12}$$

where $\hat{c}^{(\dagger)}_{\vec{r},\sigma}$ are the spin-σ electronic ladder operators, $\hat{a}^{(\dagger)}_{\vec{r}}$ denote the annihilation (creation) operators of optical phonons with frequency Ω, and the sum $\sum_{\langle\vec{r},\vec{r}'\rangle}$ is over nearest neighboring lattice sites $\vec{r},\vec{r}'$. The interaction is given by $\hat{V}_{\vec{r},\vec{r}'} = \sqrt{2M\Omega}(\hat{X}_{\vec{r}} - \hat{X}_{\vec{r}'})$ with the displacements $\hat{X}_{\vec{r}} = (1/\sqrt{2M\Omega})(\hat{a}^{\dagger}_{\vec{r}} + a_{\vec{r}})$, and we chose the oscillator mass $M = 1$ as well as $t = 1$ as the unit of energy.

Recently, this model and variations of it have gained attention due to the predicted existence of light bipolarons, which could give rise to a phonon-mediated mechanism for high-T_c superconductivity [67–70]. Unfortunately, investigating the spectral properties of Eq. (12) poses significant challenges to state-of-the-art Monte Carlo methods. TN investigations have been far out of reach; even the case of isolated bipolarons in one dimension is extremely challenging [69].

Here, we study the practically relevant case of small phonon frequencies (adiabatic limit) $\Omega/t = 0.2$ on finite lattices of size 8×8. We chose a finite Hubbard repulsion $U/t = 2$ and simulated weak and strong interactions $\lambda = (g^2/2\Omega t) = 0.025, 0.2$. In order to investigate bipolaronic quasiparticles, we computed the two-electron Green's functions,

$$G_{n,m}(\vec{k},\omega) = \langle\vec{k},n,m|\left[\hat{H} - \omega - i\eta\right]^{-1}|\vec{k},n,m\rangle, \tag{13}$$

where $|\vec{k},n,m\rangle = (1/\sqrt{L})\sum_{\vec{r}} e^{-i\vec{k}(2\vec{r}+\vec{a}_{n,m})}\hat{c}^{\dagger}_{\vec{r},\uparrow}\hat{c}^{\dagger}_{\vec{r}+\vec{a}_{n,m},\downarrow}|\varnothing\rangle$ and $\vec{a}_{n,m} = n\vec{e}_x + m\vec{e}_y$. The excitations $|\vec{k},n,m\rangle$ correspond to two-electron states with total momentum $\vec{k}$, being spatially separated by $\vec{a}_{n,m}$, and Green's functions, Eq. (13), probe the contributions of these excitations to the eigenstates of Eq. (12) [71].

We employ the projected purification [72,73] to account for the phononic Hilbert space and a single-site variant of the time-dependent variational principle to perform the time evolutions [69,74–76], using a maximum discarded weight $\delta = 10^{-10}$ and a maximum MPS bond dimension $m = 4096$. Real-time evolutions were done until a maximum time $T = 8$; longer times are practically inaccessible due to the exponential growth of the bond dimension [77]. For the complex-time evolution, we set the maximum time to $\mathrm{Re}(T_{\mathrm{cplx}}) = 64$ using time step sizes $\delta t = 0.1$ and varied the complex angle between $\alpha = 0.02\pi$ and $\alpha = 0.05\pi$.

In Fig. 2(a) we present results evaluating the imaginary part of Eq. (13) for the case of $S0$ bipolarons ($n = m = 0$) with $\lambda = 0.025$ following a high-symmetry path through the Brillouin zone (we use a broadening $\eta = 0.1$).

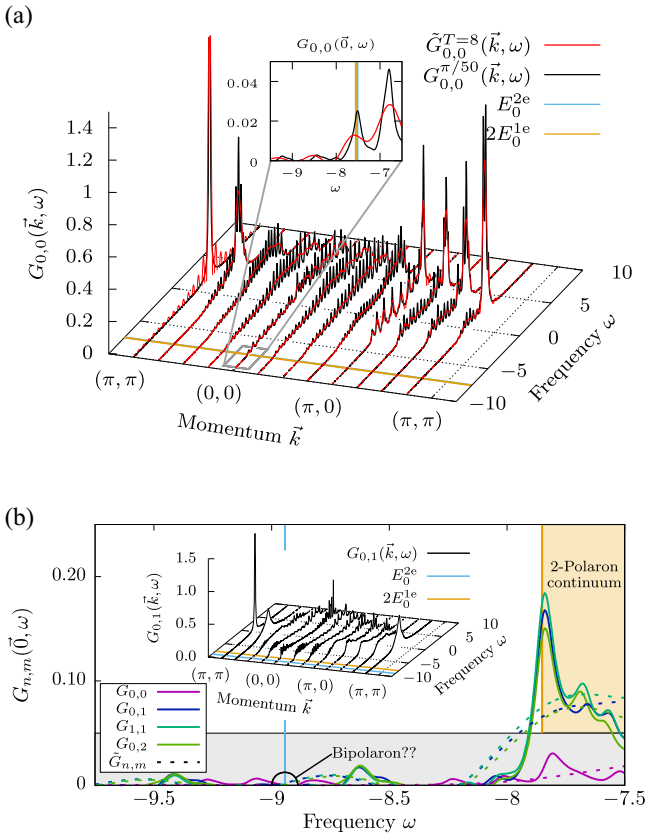


FIG. 2. (a) Comparison between uncorrected $S0$-bipolaron Green's function $\tilde{G}^{T=8}_{0,0}$ and complex-time Krylov space augmented $G^{\pi/50}_{0,0}$ with $\alpha=\pi/50$ on a 8×8 cluster for $\lambda=0.025$, following a high-symmetry path through the Brillouin zone. Note the distinct peak structure indicating dressed two-electron states, which becomes visible only when taking into account $K^T_{AB}(\omega)$. Inset: the corrected $\vec{k}=\vec{0}$ Green's function exhibits a distinguished peak right at the ground-state energy $\omega=E_0^{2e}$ computed via DMRG, which is completely washed out in $\tilde{G}^{T=8}_{0,0}$. (b) Corrected Green's functions $G^{\pi/33}_{n,m}(\vec{0},\omega)$ for different electron displacements $\vec{a}_{n,m}=n\vec{e}_x+m\vec{e}_y$ in the strong coupling regime $\lambda=0.2$ at small frequencies. The vertical blue curve indicates the two-electron ground-state energy E_0^{2e}, which is well separated from the two-polaron continuum at frequencies $\omega>2E_0^{1e}$. Above the noise threshold $R\approx 0.05$ (gray shaded area) no signal for a bipolaronic bound state can be found. Inset: $G^{\pi/33}_{0,1}(\vec{0},\omega)$ along a high-symmetry path through the Brillouin zone.

We compare the uncorrected Green's function $\tilde{G}^{T=8}_{0,0}(\vec{k},\omega)$ (red) to the complex-time corrected Green's function $G^{\pi/50}_{0,0}(\vec{k},\omega)$ (black) taking into account Eq. (8) and a complex angle $\alpha=0.02\pi$. Note the peculiar peak structure, which is completely absent in $\tilde{G}^{T=8}_{0,0}(\vec{k},\omega)$. The peaks are spaced $\approx k\Omega$ ($k\in\mathbb{N}$) and thus explicitly demonstrate the formation of polaronic bound states. We verified that the peaks are no artifacts by performing density-matrix renormalization group (DMRG) simulations. The one-(two-)electron ground-state energy E_0^{1e}/E_0^{2e} is indicated by the yellow (blue) line, and in the inset we show a close-up of the Green's functions in the vicinity of $\omega=E_0^{2e}$, for $\vec{k}=\vec{0}$ [78]. Strikingly, for the two-electron case $G^{\pi/50}_{0,0}$ shows a pronounced peak centered exactly at $\omega=E_0^{2e}$ while $\tilde{G}^{T=8}_{0,0}$ exhibits only an unspecific oscillation. Moreover, the strong peak at $\vec{k}=(\pi,\pi)$ is generated by another exact eigenstate of Eq. (12). Note how taking into account the complex-time correction mitigates artifacts in the real-time evolved Green's function and produces a smooth and sharp signal. This increase in accuracy allows for deducing that, up to finite size effects and upon evaluating the binding energy as $E_0^{2e}-2E_0^{1e}$, for weak coupling $\lambda=0.025$ there is no bipolaronic ground state. Instead, we only observe unbound two-polaron states with $w>2E_0^{1e}$, i.e., a two-polaron continuum.

The situation changes in the strong coupling regime $\lambda=0.2$ (i.e., $\lambda/\Omega=1$). In Fig. 2(b) we compare the imaginary part of the complex-time Krylov space augmented Green's functions Eq. (13) at $\vec{k}=\vec{0}$ varying the spatial separation $\vec{a}_{n,m}$ between $\vec{a}_{n,m}=(0,0)$ and $\vec{a}_{n,m}=(0,2)$, using a broadening $\eta=0.1$ and $\mathrm{Re}(T_{\mathrm{cplx}})=32$. In that case, the two-electron ground-state energy E_0^{2e} (vertical blue line) obtained via DMRG is well separated from the two-polaron continuum $2E_0^{1e}$ (yellow vertical line). Notably, we do not observe a feature at E_0^{2e} for any of the considered electron displacements $\vec{a}_{n,m}$ above the noise threshold $R\approx 0.05$, which indicates that the trial states $|\vec{k},n,m\rangle$ do not contribute significantly to the two-electron ground state. A possible explanation for this surprising finding is that the many-body ground states, if representing a bipolaron, are much more strongly correlated to their surrounding phonon clouds than previously anticipated [71]. We carefully checked in Ref. [55] that the oscillatory features visible below the noise threshold, for instance near $\omega=-8.6$, are in fact replicas, i.e., remaining artifacts not accounted for by the correction term.

Discussion and outlook—We introduced a reformulation of the Fourier transformation of a general Green's function from time to frequency domain Eq. (3), decomposing the integrand into a real-time evolution on a finite time domain and a correction $\hat{K}$. Constructing a complex-time Krylov space, we demonstrated that $\hat{K}$ can be approximated efficiently using TN methods, allowing us to overcome the Nyquist-Shannon sampling limit in frequency space. The resulting Green's functions exhibit a significantly higher accuracy, even in extremely challenging two-dimensional systems, opening the path to a precise spectral analysis of models that have been way beyond the reach of TN methods, so far. However, we expect that our method can be further improved in various ways. For instance, in this Letter we only use a fixed complex angle. Incorporating the entanglement growth along the contour could yield more efficient evolution schemes to further increase the complex-time Krylov subspace dimension. Moreover, our error analysis

suggests that direct sums of Krylov subspaces constructed from states evolved along different complex contours could drastically improve the convergence rate.

The data in this Letter were produced using SyTen [79,80] and SymMPS [81].

Acknowledgments—We thank Philipp Westhoff and John Sous for insightful discussions about the SSH model and Ulrich Schollwöck, Thomas Köhler, and Martin Grundner for carefully reading the manuscript. The author acknowledges support by the Deutsche Forschungsgemeinschaft (DFG, German Research Foundation) under Germany's Excellence Strategy-426 No. EXC-2111-390814868. This work was supported by Grant No. INST 86/1885-1 FUGG of the German Research Foundation (DFG).

Data availability—The data that support the findings of this article are not publicly available upon publication because it is not technically feasible and/or the cost of preparing, depositing, and hosting the data would be prohibitive within the terms of this research project. The data are available from the authors upon reasonable request.

[1] H. Benthien, F. Gebhard, and E. Jeckelmann, Spectral function of the one-dimensional hubbard model away from half filling, Phys. Rev. Lett. **92**, 256401 (2004).
[2] S. R. White and I. Affleck, Spectral function for the $s = 1$ Heisenberg antiferromagetic chain, Phys. Rev. B **77**, 134437 (2008).
[3] R. G. Pereira, S. R. White, and I. Affleck, Spectral function of spinless fermions on a one-dimensional lattice, Phys. Rev. B **79**, 165113 (2009).
[4] M. Mourigal, M. Enderle, A. Klöpperpieper, J.-S. Caux, A. Stunault, and H. M. Rønnow, Fractional spinon excitations in the quantum Heisenberg antiferromagnetic chain, Nat. Phys. **9**, 435 (2013).
[5] M. Weber, F. F. Assaad, and M. Hohenadler, Phonon spectral function of the one-dimensional Holstein-Hubbard model, Phys. Rev. B **91**, 235150 (2015).
[6] M. Gohlke, R. Verresen, R. Moessner, and F. Pollmann, Dynamics of the Kitaev-Heisenberg model, Phys. Rev. Lett. **119**, 157203 (2017).
[7] A. Keselman, C. Murthy, B. van Heck, and B. Bauer, Spectral response of Josephson junctions with low-energy quasiparticles, SciPost Phys. **7**, 050 (2019).
[8] F. Grusdt, E. Demler, and A. Bohrdt, Pairing of holes by confining strings in antiferromagnets, SciPost Phys. **14**, 090 (2023).
[9] M. c. v. Kebrič, J. C. Halimeh, U. Schollwöck, and F. Grusdt, Confinement in $(1 + 1)$-dimensional $\mathbb{z}_2$ lattice gauge theories at finite temperature, Phys. Rev. B **109**, 245110 (2024).
[10] H. R. Krishna-murthy, J. W. Wilkins, and K. G. Wilson, Renormalization-group approach to the anderson model of dilute magnetic alloys (part i + part ii), Phys. Rev. B **21**, 1003 (1980).
[11] A. Georges, G. Kotliar, W. Krauth, and M. J. Rozenberg, Dynamical mean-field theory of strongly correlated fermion systems and the limit of infinite dimensions, Rev. Mod. Phys. **68**, 13 (1996).
[12] R. Bulla, A. C. Hewson, and T. Pruschke, Numerical renormalization group calculations for the self-energy of the impurity Anderson model, J. Phys. Condens. Matter **10**, 8365 (1998).
[13] G. Kotliar, S. Y. Savrasov, K. Haule, V. S. Oudovenko, O. Parcollet, and C. A. Marianetti, Electronic structure calculations with dynamical mean-field theory, Rev. Mod. Phys. **78**, 865 (2006).
[14] M. Potthoff, M. Aichhorn, and C. Dahnken, Variational cluster approach to correlated electron systems in low dimensions, Phys. Rev. Lett. **91**, 206402 (2003).
[15] M. Potthoff, Self-energy-functional approach to systems of correlated electrons, Eur. Phys. J. B **32**, 429 (2003).
[16] M. Potthoff, Self-energy-functional approach: Analytical results and the Mott-Hubbard transition, Eur. Phys. J. B **36**, 335 (2003).
[17] C. Dahnken, M. Aichhorn, W. Hanke, E. Arrigoni, and M. Potthoff, Variational cluster approach to spontaneous symmetry breaking: The itinerant antiferromagnet in two dimensions, Phys. Rev. B **70**, 245110 (2004).
[18] P. Werner and A. J. Millis, Efficient dynamical mean field simulation of the Holstein-Hubbard model, Phys. Rev. Lett. **99**, 146404 (2007).
[19] T. E. Reinhard, U. Mordovina, C. Hubig, J. S. Kretchmer, U. Schollwöck, H. Appel, M. A. Sentef, and A. Rubio, Density-matrix embedding theory study of the one-dimensional hubbard–holstein model, J. Chem. Theory Comput. **15**, 2221 (2019).
[20] G. Bollmark, T. Köhler, L. Pizzino, Y. Yang, J. S. Hofmann, H. Shi, S. Zhang, T. Giamarchi, and A. Kantian, Solving 2d and 3d lattice models of correlated fermions—Combining matrix product states with mean-field theory, Phys. Rev. X **13**, 011039 (2023).
[21] B. Lenz, C. Martins, and S. Biermann, Spectral functions of Sr_2IrO_4: Theory versus experiment, J. Phys. Condens. Matter **31**, 293001 (2019).
[22] J. Karp, A. Hampel, and A. J. Millis, Superconductivity and antiferromagnetism in $NdNiO_2$ and $CaCuO_2$: A cluster DMFT study, Phys. Rev. B **105**, 205131 (2022).
[23] M. Bramberger, J. Mravlje, M. Grundner, U. Schollwöck, and M. Zingl, $BaOSo_3$: A Hund's metal in the presence of strong spin-orbit coupling, Phys. Rev. B **103**, 165133 (2021).
[24] M. Bramberger, B. Bacq-Labreuil, M. Grundner, S. Biermann, U. Schollwöck, S. Paeckel, and B. Lenz, Formation of CuO_2 sublattices by suppression of interlattice correlations in tetragonal CuO, SciPost Phys. **14**, 010 (2023).
[25] S. Paeckel, T. Köhler, S. R. Manmana, and B. Lenz, Matrix-product-state-based Band-Lanczos solver for quantum cluster approaches, Phys. Rev. B **112**, 235108 (2025).
[26] M. Grundner, F. B. Kugler, O. Parcollet, U. Schollwöck, A. Georges, and A. Hampel, LiV_2O_4: Hund-assisted orbital-selective mottness, Phys. Rev. B **112**, L041106 (2025).
[27] E. Fradkin, *Field Theories of Condensed Matter Physics* (Cambridge University Press, Cambridge, England, 2013).

[28] F. Aryasetiawan and O. Gunnarsson, The GW method, Rep. Prog. Phys. **61**, 237 (1998).
[29] G. Onida, L. Reining, and A. Rubio, Electronic excitations: Density-functional versus many-body Green's-function approaches, Rev. Mod. Phys. **74**, 601 (2002).
[30] J. Reuther and R. Thomale, Functional renormalization group for the anisotropic triangular antiferromagnet, Phys. Rev. B **83**, 024402 (2011).
[31] W. Metzner, M. Salmhofer, C. Honerkamp, V. Meden, and K. Schönhammer, Functional renormalization group approach to correlated fermion systems, Rev. Mod. Phys. **84**, 299 (2012).
[32] N. Dupuis, L. Canet, A. Eichhorn, W. Metzner, J. Pawlowski, M. Tissier, and N. Wschebor, The nonperturbative functional renormalization group and its applications, Phys. Rep. **910**, 1 (2021).
[33] T. D. Kühner and S. R. White, Dynamical correlation functions using the density matrix renormalization group, Phys. Rev. B **60**, 335 (1999).
[34] R. Bulla, The numerical renormalization group method for correlated electrons, in *Advances in Solid State Physics 40*, edited by B. Kramer (Springer, Berlin, Heidelberg, 2000), pp. 169–182.
[35] M. Aichhorn, M. Daghofer, H. G. Evertz, and W. von der Linden, Low-temperature Lanczos method for strongly correlated systems, Phys. Rev. B **67**, 161103(R) (2003).
[36] A. Weichselbaum and J. von Delft, Sum-rule conserving spectral functions from the numerical renormalization group, Phys. Rev. Lett. **99**, 076402 (2007).
[37] R. Bulla, T. A. Costi, and T. Pruschke, Numerical renormalization group method for quantum impurity systems, Rev. Mod. Phys. **80**, 395 (2008).
[38] S. R. White, Density matrix formulation for quantum renormalization groups, Phys. Rev. Lett. **69**, 2863 (1992).
[39] U. Schollwoeck, The density-matrix renormalization group in the age of matrix product states, Ann. Phys. (Amsterdam) **326**, 96 (2010).
[40] N. V. Prokof'ev and B. V. Svistunov, Polaron problem by diagrammatic quantum monte carlo, Phys. Rev. Lett. **81**, 2514 (1998).
[41] K. Van Houcke, E. Kozik, N. Prokof'ev, and B. Svistunov, Diagrammatic monte carlo, Phys. Procedia **6**, 95 (2010).
[42] J. Eisert, M. Cramer, and M. B. Plenio, Colloquium: Area laws for the entanglement entropy, Rev. Mod. Phys. **82**, 277 (2010).
[43] J. Eisert, M. Friesdorf, and C. Gogolin, Quantum many-body systems out of equilibrium, Nat. Phys. **11**, 124 (2015).
[44] E. H. Lieb and D. W. Robinson, The finite group velocity of quantum spin systems, Commun. Math. Phys. **28**, 251 (1972).
[45] H. Nyquist, Certain topics in telegraph transmission theory, Trans. Am. Inst. Electr. Eng. **47**, 617 (1928).
[46] C. E. Shannon, Communication in the presence of noise, Proc. IRE **37**, 10 (1949).
[47] E. Candes and T. Tao, Decoding by linear programming, IEEE Trans. Inf. Theory **51**, 4203 (2005).
[48] E. J. Candès, J. K. Romberg, and T. Tao, Stable signal recovery from incomplete and inaccurate measurements, Commun. Pure Appl. Math. **59**, 1207 (2006).
[49] C. Lánczos, An iterative method for the solution of the eigenvalue problem of linear differential and integral, J. Res. Natl. Bur. Stand. **45**, 225 (1950).
[50] J. K. Cullum and R. A. Willoughby, *Lanczos Algorithms for Large Symmetric Eigenvalue Computations*, Vol. 1 (Progress in Scientific Computing, Basel, Switzerland, 1985).
[51] R. W. Freund, Band lanczos method, in *Templates for the Solution of Algebraic Eigenvalue Problems: A Practical Guide*, edited by Z. Bai, J. D. Demmel, A. Ruhe, J. Dongarra, and H. van der Vorst (SIAM, Philadelphia, 2000), Chap. 4.6, pp. 80–88.
[52] M. Grundner, P. Westhoff, F. B. Kugler, O. Parcollet, and U. Schollwöck, Complex time evolution in tensor networks and time-dependent Green's functions, Phys. Rev. B **109**, 155124 (2024).
[53] X. Cao, Y. Lu, E. M. Stoudenmire, and O. Parcollet, Dynamical correlation functions from complex time evolution, Phys. Rev. B **109**, 235110 (2024).
[54] S. Paeckel, T. Köhler, A. Swoboda, S. R. Manmana, U. Schollwöck, and C. Hubig, Time-evolution methods for matrix-product states, Ann. Phys. (Amsterdam) **411**, 167998 (2019).
[55] See Supplemental Material at http://link.aps.org/supplemental/10.1103/bx76-hps4 for a detailed error analysis, which includes Refs. [56–59].
[56] M. Hochbruck and C. Lubich, On Krylov subspace approximations to the matrix exponential operator, SIAM J. Numer. Anal. **34**, 1911 (1997).
[57] M. Hochbruck and C. Lubich, Exponential integrators for quantum-classical molecular dynamics, BIT **39**, 620 (1999).
[58] E. M. Stoudenmire and S. R. White, Real-space parallel density matrix renormalization group, Phys. Rev. B **87**, 155137 (2013).
[59] Y. Shen, K. Klymko, J. Sud, D. B. Williams-Young, W. A. d. Jong, and N. M. Tubman, Real-time Krylov theory for quantum computing algorithms, Quantum **7**, 1066 (2023).
[60] Bringing $\mathbf{H}_{\text{eff}}$ into the upper Hessenberg form directly allows for reading of the matrix element $h_{r,r-1}$.
[61] S. R. White, Density-matrix algorithms for quantum renormalization groups, Phys. Rev. B **48**, 10345 (1993).
[62] U. Schollwöck, The density-matrix renormalization group, Rev. Mod. Phys. **77**, 259 (2005).
[63] U. Schollwöck, The density-matrix renormalization group in the age of matrix product states, Ann. Phys. (Amsterdam) **326**, 96 (2011).
[64] S. Barišić, Rigid-atom electron-phonon coupling in the tight-binding approximation. I, Phys. Rev. B **5**, 932 (1972).
[65] S. Barišić, Self-consistent electron-phonon coupling in the tight-binding approximation. II, Phys. Rev. B **5**, 941 (1972).
[66] W. P. Su, J. R. Schrieffer, and A. J. Heeger, Solitons in polyacetylene, Phys. Rev. Lett. **42**, 1698 (1979).
[67] J. Sous, M. Chakraborty, R. V. Krems, and M. Berciu, Light bipolarons stabilized by Peierls electron-phonon coupling, Phys. Rev. Lett. **121**, 247001 (2018).
[68] C. Zhang, J. Sous, D. R. Reichman, M. Berciu, A. J. Millis, N. V. Prokof'ev, and B. V. Svistunov, Bipolaronic high-temperature superconductivity, Phys. Rev. X **13**, 011010 (2023).

[69] M. Grundner, T. Blatz, J. Sous, U. Schollwöck, and S. Paeckel, Cooper-paired bipolaronic superconductors, arXiv: 2308.13427.

[70] K.-S. Kim, Z. Han, and J. Sous, Semiclassical theory of bipolaronic superconductivity in a bond-modulated electron-phonon model, Phys. Rev. B **109**, L220502 (2024).

[71] M. Berciu, Few-particle Green's functions for strongly correlated systems on infinite lattices, Phys. Rev. Lett. **107**, 246403 (2011).

[72] T. Köhler, J. Stolpp, and S. Paeckel, Efficient and flexible approach to simulate low-dimensional quantum lattice models with large local Hilbert spaces, SciPost Phys. **10**, 058 (2021).

[73] J. Stolpp, T. Köhler, S. R. Manmana, E. Jeckelmann, F. Heidrich-Meisner, and S. Paeckel, Comparative study of state-of-the-art matrix-product-state methods for lattice models with large local Hilbert spaces without U(1) symmetry, Comput. Phys. Commun. **269**, 108106 (2021).

[74] J. Haegeman, J. I. Cirac, T. J. Osborne, I. Pižorn, H. Verschelde, and F. Verstraete, Time-dependent variational principle for quantum lattices, Phys. Rev. Lett. **107**, 070601 (2011).

[75] J. Haegeman, C. Lubich, I. Oseledets, B. Vandereycken, and F. Verstraete, Unifying time evolution and optimization with matrix product states, Phys. Rev. B **94**, 165116 (2016).

[76] M. Yang and S. R. White, Time-dependent variational principle with ancillary Krylov subspace, Phys. Rev. B **102**, 094315 (2020).

[77] In fact, the maximum time $T = 8$ could be reached only for a few initial states due to the rapid growth of memory requirements.

[78] Because of the finite cluster size there are strong finite size effects. We checked this by computing the ground state of the non interacting model yielding a ground -state energy, which is always larger than the one obtained when incorporating finite λ.

[79] C. Hubig, F. Lachenmaier, N.-O. Linden, T. Reinhard, L. Stenzel, A. Swoboda, M. Grundner, S. Mardazad, and S. Paeckel, The SyTen toolkit, https://syten.eu/.

[80] C. Hubig, Symmetry-protected tensor networks, Ph.D. thesis, LMU München, 2017).

[81] S. Paeckel and T. Köhler, SymMPS, https://www.symmps.eu, accessed: 2019-12-29.